AGU ADVANCING EARTH AND SPACE SCIENCE

Geophysical Research Letters®

RESEARCH LETTER
10.1029/2021GL097323

Key Points:

- Subsolidus fayalitic olivine decomposition forming unique vesicular nanophase iron particles in Chang'E-5 soils was confirmed
- Nanophase iron particles in the uppermost olivine layer are embedded with numerous vesicles containing possible O_2 or SiO component
- Unique microstructural features on fayalitic olivine rims shed light on the diversity of space weathering effects on the lunar surface

Supporting Information:

Supporting Information may be found in the online version of this article.

Correspondence to:

Y. Li,
liyang@mail.gyig.ac.cn

Citation:

Guo, Z., Li, C., Li, Y., Wen, Y., Tai, K., Li, X., et al. (2022). Nanophase iron particles derived from fayalitic olivine decomposition in Chang'E-5 lunar soil: Implications for thermal effects during impacts. *Geophysical Research Letters*, *49*, e2021GL097323. https://doi.org/10.1029/2021GL097323

Received 14 DEC 2021
Accepted 15 FEB 2022

Author Contributions:

Conceptualization: Zhuang Guo
Formal analysis: Chen Li
Funding acquisition: Yang Li, Jianzhong Liu
Investigation: Kairui Tai
Methodology: Zhuang Guo, Yuanyun Wen
Project Administration: Yang Li
Software: Chen Li
Supervision: Yang Li, Xiongyao Li, Jianzhong Liu, Ziyuan Ouyang
Writing – original draft: Zhuang Guo

Nanophase Iron Particles Derived From Fayalitic Olivine Decomposition in Chang'E-5 Lunar Soil: Implications for Thermal Effects During Impacts

Zhuang Guo[1,2], Chen Li[1,3], Yang Li[1,4], Yuanyun Wen[1], Kairui Tai[1,5], Xiongyao Li[1,4], Jianzhong Liu[1,4], and Ziyuan Ouyang[1]

[1]Center for Lunar and Planetary Sciences, Institute of Geochemistry, Chinese Academy of Sciences, Guiyang, China, [2]College of Earth and Planetary Sciences, University of Chinese Academy of Sciences, Beijing, China, [3]Faculty of Metallurgical and Energy Engineering, Kunming University of Science and Technology, Kunming, China, [4]Center for Excellence in Comparative Planetology, Chinese Academy of Sciences, Hefei, China, [5]Department of Geology, Northwest University, Xi'an, China

Abstract Surface-correlated nanophase iron particles ($npFe^0$) alter the reflectance spectrum characteristics of airless bodies, thus making it an essential aspect of studying space weathering. Vapor deposition has been the only strongly proven $npFe^0$ formation mechanism owing to the long exposure time of Apollo samples, whereas other formation mechanisms remain questioned. Newly returned younger Chang'E-5 samples provide an opportunity to study the incipient formation mechanism of $npFe^0$. Here, we combined transmission electron microscopy and electron energy loss spectroscopy to characterize the microscopic features of Chang'E-5 olivine rims. The uppermost layer of these grains exhibits the simultaneous coexistence of $npFe^0$ with Si-rich material overlying an Mg-rich layer, as well as numerous irregular vesicles containing oxygen-rich (SiO and O_2) components embedded in the $npFe^0$. These microscopic features collectively suggest subsolidus olivine decomposition during (micro)impact-induced fragmentation or local heating processes, which may be the essential agent to alter the reflectance spectrum of airless bodies.

Plain Language Summary Airless bodies experienced a space weathering modification to form the nanophase iron particles ($npFe^0$) that would alter the reflectance spectrum. However, the formation mechanism of $npFe^0$ remains controversial due to the lack of less-exposed lunar samples to study the incipient information about $npFe^0$ formation, except for the widely accepted vapor deposition origin. Our study is based on the younger Chang'E-5 samples and report the first strong evidence of unique vesicular $npFe^0$ produced by olivine decomposition under subsolidus conditions, which may be the first effect contributing to $npFe^0$ formation on the lunar surface. This formation mechanism will shed light on the $npFe^0$ production and further broaden the perspective of impact effects beyond the Moon and deepen the current understanding of unexplored celestial bodies using remote sensing.

1. Introduction

Space weathering actively occurs on the surfaces of both the Moon and asteroids. Microscopic space weathered features have been well characterized in returned samples, thus providing essential information for understanding the evolution of regolith on airless bodies (Keller & McKay, 1997; Noguchi et al., 2011; Pieters & Noble, 2016). Surface-correlated nanophase iron particles ($npFe^0$) products related to space weathering significantly affect the optical properties of the airless body surfaces, mainly darkening and reddening the visible to near-infrared reflectance spectrum, which may obscure their true mineralogical constituents (Anand et al., 2004; Chapman, 2004; Gaffey, 2010; Hapke, 2001).

A combination of laboratory-simulated experiments and returned sample analyses (Apollo and Itokawa samples) indicates that there are mainly two mechanisms for $npFe^0$ formation: (a) H reduction of Fe-bearing silicate melts; and (b) the evaporation and deposition of elemental iron on the surface of lunar soil grains by energetic micrometeorite impacts or ion-particle sputtering (Basu, 2005; Fazio et al., 2018; Hapke et al., 1975; Loeffler et al., 2009; Sasaki et al., 2001; Weber et al., 2020; Yamada et al., 1999). However, older Apollo samples have long exposure ages, which means that extensive micrometeorite impacts and energetic solar wind have acted on their surfaces, and the initial morphology and chemical composition of the weathered rims were likely significantly altered

(Keller & McKay, 1997; Pieters & Noble, 2016; Thompson, 2021). In particular, the H reduction origin is questioned because there is no direct evidence for by-product (e.g., H_2O, SiO_2) production in the rims, and laser irradiation experiments perfectly reproduce npFe^0-containing rims in the absence of hydrogen (Fazio et al., 2018; Sasaki et al., 2001; Weber et al., 2020).

Many experiments have shown that nondeposited npFe^0 can be extracted from mafic silicate at high temperature, but no clear formation mechanism has been determined from the returned samples (Fazio et al., 2018). Some thermal-induced metallic iron particles (disproportionation reaction and decomposition of mafic silicate) have also been recognized in meteorites (Guo et al., 2020, 2021; van de Moortele et al., 2007).

On December 17, 2020, Chang'E-5 successfully returned the new younger lunar regolith sample from Mons Rümker located in northern Oceanus Procellarum to Earth. The evolution processes (excavation, mixing, burial, transport) of lunar regolith make it likely that younger Chang'E-5 lunar soils will have a very short surface residence time (O'Brien & Byrne, 2021). The excavation ages of most studied regolith are estimated to be several tens of Ma and linked to the Xu Guangqi (IC-396) and IC-265 craters (Qian et al., 2021). Based on the youngest exposure ages of Chang'E-5 shovel samples, our work focuses on characterizing the olivine rims to better understand the initial reaction information of the lunar surface processes. Here, we give strong evidence for the exact thermally induced formation of npFe^0. This is important for further broadening the perspective on impact effects beyond the Moon and for rationalizing the current understanding of unexplored celestial bodies using remote sensing.

2. Materials and Methods

Since the fine fraction of lunar soil always has more surface-correlated npFe^0 to alter the optical properties of the bulk soil (Noble et al., 2001; Pieters et al., 1993). Samples carried out in our study are shoveled fine fractions of the topmost surface of Chang'E-5 landing site, labeled as CE5C0400YJFM00505.

A small amount of Chang'E-5 grains was spread on sticky silicon tape and covered with an Au film for scanning electron microscope (SEM) observation, and the prepared samples were stored under vacuum conditions. Three single olivine grains and one multiphase clastic grain, ranging in size from ∼10 to 20 μm, were identified using a FEI Scios field-emission SEM equipped with an energy dispersive X-ray spectrometer (EDS) housed at the Institute of Geochemistry, Chinese Academy of Sciences (CAS), Guiyang. Transmission electron microscope (TEM) samples of each grain were extracted using a focused ion beam (FIB) following the FEI dual beam method, and these sections were thinned to less than 100 nm to reduce the analytical artifacts. The TEM samples were characterized using an FEI Talos F200X field-emission scanning transmission electron microscope (FE-STEM) operating at 200 kV at the Suzhou Institute of Nano-tech and Nano-bionics, CAS. Chemical analysis of the region of interest on the FIB sections was carried out using an EDS detector on the STEM instrument. High-resolution (HR)TEM images and selected area electron diffraction (SAED) patterns were obtained to confirm the nanoscale crystal structure.

Electron energy loss spectroscopy (EELS) spectra were obtained using a Gatan GIF Quantum ER System Model 965 parallel EELS spectrometer attached to a Hitachi HF5000 aberration-corrected STEM housed at the Shanghai Institute of Ceramics, CAS, operating at an accelerating voltage of 200 kV. In our study, synthetic fayalite, terrestrial hematite, and FeNi metal from an ordinary chondrite meteorite (GRV 051874) were prepared as Fe^{2+}, Fe^{3+}, and Fe^0 reference standards, respectively, for the EELS analysis. The energy resolution of the EELS measurement is 0.5–0.7 eV, which was calculated from the FWHM of the zero-loss peak. The EELS spectral images (SI) were obtained in DualEELS mode with a probe current of 100 pA. Acquisition times were 10 s for Fe and O point analyses, 18 s for Fe and O analyses at each point in the line-scan, 40 s for Si point analyses, and 72 s for line-scans of Si at each point.

Factsage is one of the World's largest fully integrated database computing systems for chemical thermodynamics. To constrain the olivine decomposition reaction conditions, the thermodynamic calculations of the reaction formulas ($Fe_2SiO_4 = 2Fe + SiO_2 + O_2$ and $Fe_2SiO_4 = 2Fe + SiO + 3/2O_2$) were made using Factsage 8.0. The FactPS database was used for the gas and pure substances, and the FToxid database was used for olivine. The Gibbs free energies of the two decomposition reactions of olivine under different vacuum conditions (10^{-9} to 10^{-12} Pa) were calculated in the nonstandard state.

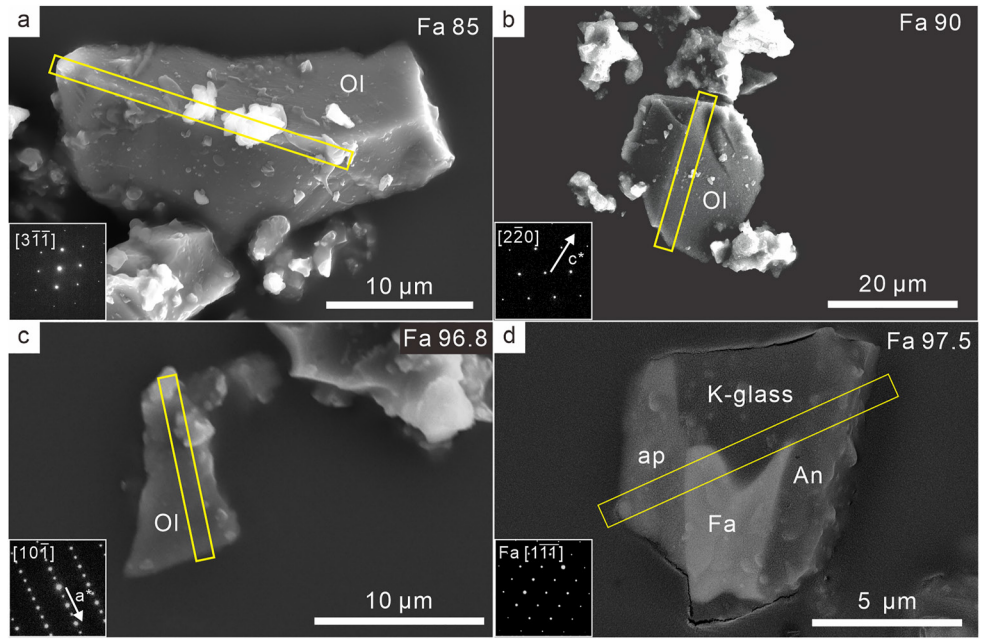

Figure 1. Scanning electron microscope (SEM) images of the studied grains selected from the fine fraction of the Chang'E-5 lunar soils. (a–c) Secondary electronic images of single olivine (Ol) grains with diverse Fa values. (d) Backscattered electron image of a lithic fragment composed of apatite (ap) + fayalite (Fa) + K-rich glass (K-glass) + anorthite (An). The yellow rectangles indicate the extraction locations of the focused ion beam (FIB) samples. The selected area electron diffraction (SAED) pattern corresponding to each olivine grain is shown in the lower-left corner of each image.

3. Results

Three single Fe-rich olivine grains and one fayalite-bearing clastic fragment were selected for study according to their compositions obtained using an SEM equipped with an EDS, and these selected grains have a relatively clean surface with no obvious agglutinate glasses or splashed melt. Each olivine crystal was further verified using the SAED patterns from the TEM analysis (Figure 1). The average composition of each host grain was determined by STEM-EDS, yielding diverse Fa values (Fa 85, Fa 90, Fa 96.8, and Fa 97.5; Table S1 in Supporting Information S1). We use the Fa values to represent the corresponding olivine grains in the following text.

3.1. Microscopic Features of Olivine Rims

The TEM observations show that these grains have ~100-nm-thick continuous rims, and no melt layer is observed (Figure 2 and Figures S1, S2 in Supporting Information S1). Strictly speaking, the rims observed on the surface of the olivine crystals fall into the category of multiple rims classified by Keller and McKay (1997), which is described as an inclusion-rich layer on top of a partially to completely radiation-damaged amorphous layer, which suggests that rim formation involves multiple processes (Figure 2; Keller & McKay, 1997).

Quantitative TEM-EDX compositional maps and line profiles were obtained from the rim of each grain. The microscopic features of the uppermost layer simultaneously exhibit the coexistence of vesicular npFe^0 and Si-rich material covering an Mg-rich layer (Figure 1f). The partially amorphous inner layer with a thickness of a few tens of nanometers presents an irregular boundary with the underlying grains, referred to as the solar wind layer, that shows an identical composition and crystallographic orientation as the host grain, which is attributed to solar wind ion irradiation effects (Figures 1c and 1f; Noguchi et al., 2014). Dense solar flare tracks are observed in the host grain interiors (Figure 2 and Figures S1, S2 in Supporting Information S1). The origin of npFe^0 is our primary concern, and detailed information regarding the uppermost layer is described as follows.

The npFe^0 and Si-rich material are regularly arranged horizontally in the uppermost inclusion-rich layer of these olivine grains, and the composition of the uppermost layer substantially differs from that of the host minerals (Figure 2f and Figures S1, S2 in Supporting Information S1). The Si-rich material (interstitial between npFe^0

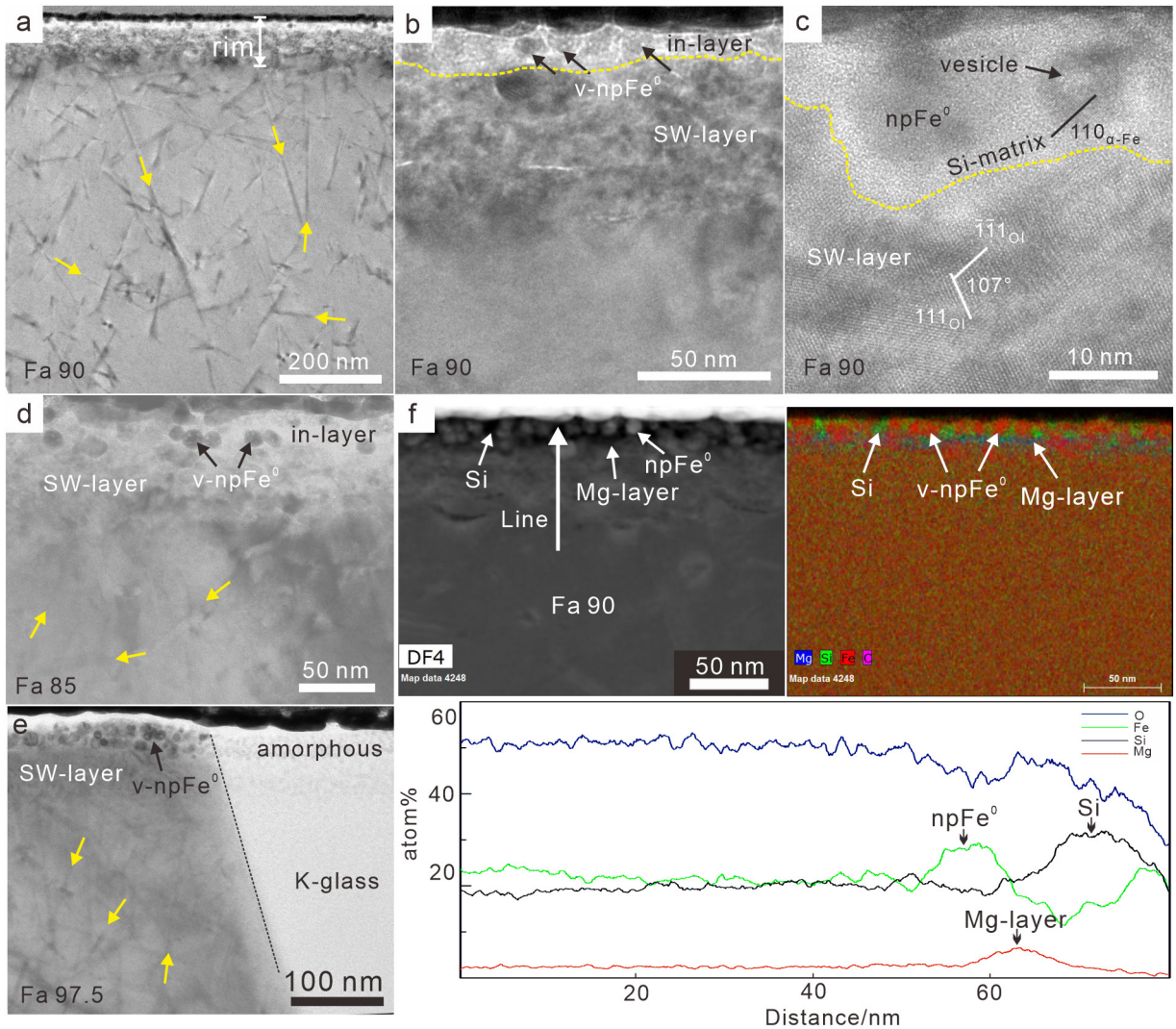

Figure 2. (a–c) Transmission electron microscope (TEM) bright-field and high-resolution TEM images of the Fa 90 olivine grain, showing an approximately 80-nm-thick rim and abundant vesicular npFe^0 (v-npFe^0) particles embedded in the uppermost inclusion layer (in-layer). (d) TEM bright-field image of the Fa 85 olivine grain, showing a ~70-nm-thick rim with a similar microstructure to that of Fa 90. (e) Multiphase TEM bright-field image from a clastic fragment with the inclusion layer appearing only on the top of the Fa 97.5 olivine grain and absent on the adjacent K-rich glassy grain. (f) High-angle annular dark-field (HAADF) image of a part of the Fa 90 olivine rim and corresponding quantitative energy dispersive X-ray spectrometer element map. The line profile results are obtained from the arrow position in the HAADF image. The chemical composition suggests that the uppermost layer is characterized by vesicular npFe^0 (v-npFe^0) particles embedded in an Si-rich matrix (Si) overlying an Mg-rich layer, whereas the solar wind layer has a consistent composition with the substrate olivine. Yellow arrows represent the presence of solar flare tracks within the host olivine.

particles) is Si, Mg-rich, and O-poor relative to the host olivine, with no significant foreign elements (e.g., S, Ca, and Al) detected in the uppermost layer (Figure 2f and Figure S1 in Supporting Information S1). The average atomic percentages of the Si-rich material in Fa 90 are: O, 47.9% (53.9%); Si, 23.67% (13.78%); Mg, 5.06% (2.90%); Fe, 16.19% (25.72%); Al, 1.86% (0.73%); Ca, 1.53% (0.47%); and S, 1.35% (0.80%), where the values in brackets are the compositional data from the host olivine (Table S1 in Supporting Information S1).

Spherical and angular npFe^0 particles, ranging in size from 10 to 35 nm, are widely dispersed in this layer, especially a rhombohedral α-iron particle (~35 nm) that appear at the Fa 97 rim (Figure 3d and Figure S2 in Supporting Information S1). In addition to the Si-rich matrix, some npFe^0 particles are also embedded in the Mg-rich layer, indicating a close relationship with the various chemical components in the uppermost layer (Figure 3d). These npFe^0 particles are extremely enriched in iron, with no sulfur or nickel, and HRTEM images further identify them as α-Fe (Figure 3e and Figures S1–S3 in Supporting Information S1). Each phase on the multiphase

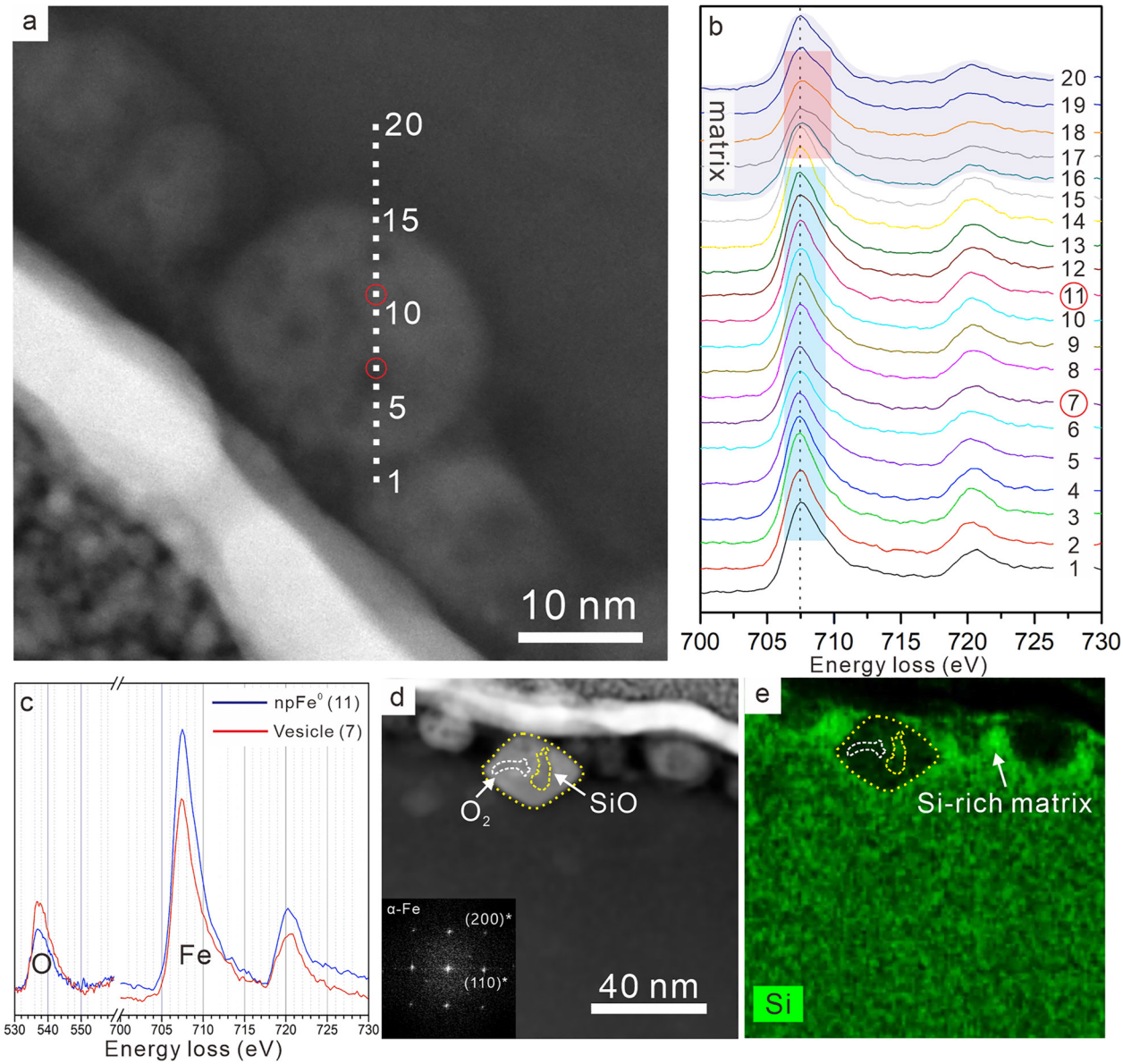

Figure 3. (a) Close-up high-angle annular dark-field (HAADF) image of vesicular npFe^0 in Fa 96.8, showing the location of the electron energy loss spectroscopy (EELS) line-scan (white dotted line crosscuts the npFe^0, vesicle, and matrix). Each white dot suggests the position of the point analysis corresponding to the spectra of Figure 3b from 1 to 20. (b) EELS spectrum of Fe from the line-scan. Inside the npFe^0 particle (points 1–15), the Fe L_3 peak shows a consistent full width at half maximum (FWHM, blue translucent rectangle), which is distinct from the matrix (pink translucent rectangle). (c) Two EELS spectra of Fe and O extracted from the line-scan (points 7 and 11) and vesicle (point 7) showing significant oxygen enrichment. The Fe spectra were processed by removing the background using the first Order Log-Polynomial method in Digital Micrograph software. (d) HAADF image of a large rhombohedral vesicular npFe^0 in Fa 96.8. The fast Fourier transform pattern of this grain is shown in the lower-left corner. (d) TEM-EDX Si elemental map of (c), indicating both a Si-bearing (yellow dotted line) and Si-poor (white dotted lines) component in these vesicles embedded in the npFe^0.

fragment should experience the same conditions, but npFe^0 only appears on the top of the olivine grain (Fa 97.5), indicating a phase-dependent origin of such npFe^0 (Figure 2e).

Another unique microstructure of these npFe^0 is that almost all of the particles are vesicular. EELS is an effective method for determining the contents of vesicles and the Fe valence state at the nanoscale in extraterrestrial samples (Burgess & Stroud, 2018b; Garvie & Buseck, 1998). We used STEM with EELS to examine the detailed chemical characteristics on the rims of these particles. EELS spectra and high-magnification TEM-EDX mapping were acquired to confirm the components trapped in these vesicles (Figures 2 and 3).

The peak energy position of Fe-L_3 from the EELS line-scan through the npFe^0 grain is located at 707.5 eV, which is consistent with the standards (FeNi: Fe^0; fayalite: Fe^{2+}) and previous studies, and the full width at half maximum (FWHM) of Fe^0 at the ~707.5 eV peak is generally greater than those of Fe^{2+}-bearing silicates (Figure 3b and Figure S4 in Supporting Information S1) (Garvie & Buseck, 1998). The EELS line-scan result shows an approximately uniform Fe-L_3 FWHM (~3.02 eV) within the vesicular npFe^0 grain, while the matrix shows a greater FWHM (~3.44 eV) at the ~708 eV peak (Figure 3b and Figure S5 in Supporting Information S1). The greater FWHM of the matrix is inconsistent with that of the fayalite standard (~2.7 eV), which may suggest a slight oxidation of the amorphous matrix during TEM analysis, and the presence of Fe^{3+} may have broadened the Fe EELS peaks at ~708 eV. The EELS spectra of O from the npFe^0 and trapped vesicles shows that the vesicle positions exhibit higher O components, whereas helium from the solar wind is not detected in the vesicles (Figure 3c and Figure S6 in Supporting Information S1). The TEM-EDX mapping and EELS spectra of Si also indicate that the vesicles trapped in the npFe^0 are dichotomous, with both Si-rich and Si-poor features in these vesicle positions (Figures 3d, 3e and Figure S7 in Supporting Information S1).

4. Discussion

4.1. Formation Mechanism of npFe^0

Olivine grains from Chang'E-5 grains simultaneously show the coexistence of vesicular npFe^0 with Si-rich material and an underlying Mg-rich layer (Figure 2f). These microscopic features indicate that Chang'E-5 olivines should have experienced a common event in the lunar environment and exhibit a similar npFe^0 formation mechanism.

Spherical npFe^0 in the uppermost layers of lunar grains with a mean size of 3 nm has traditionally been thought to have formed from vapor redeposition caused by micrometeorite impact or energetic ion-particle sputtering (Keller & McKay, 1993, 1997; Weber et al., 2020). However, the morphology of the npFe^0 (e.g., considerably larger, nonspherical, up to 35 nm), microchemical distribution (e.g., absence of foreign volatile elements), and phase-dependence features (e.g., npFe^0 only appear on Fe-bearing minerals) of the Chang'E-5 olivine rims are distinct from those of well-known features in the returned Apollo and Itokawa samples, and their origin cannot be explained by vapor deposition (Hapke, 2001; Keller & McKay, 1997).

In our multiphase clastic fragment, we did not observe an olivine-like inclusion-rich layer on the adjacent Fe-free phase (K-glass), which supports that the uppermost inclusion layer in the Chang'E-5 olivine is phase dependent and that the npFe^0 particles should have directly formed from the host olivine grain.

Pure iron produced from olivine under thermal conditions has been proved in meteorites, given the reaction: $Fe_2SiO_4 = 2Fe + xSiO_2 + (1 - x)\,SiO + (3 - x)/2O_2$ (Leroux et al., 2003). In the rim of Chang'E-5 olivine grains, the presence of vesicular npFe^0 associated with Si-rich material and an Mg-rich layer in the olivine grain rims is recognized by TEM analysis. Based on their close spatial and chemical distribution, we propose that their formation is linked to olivine decomposition. The quantitative EDS analysis results of the Mg-rich layer and Si-rich matrix both show significant Fe depletion compared with the host olivine, which provides a material basis for the formation of npFe^0 (Figure 2f). As discussed above, olivine decomposition is the most reasonable reaction available to form the unique microstructure of the uppermost layer of the Chang'E-5 fayalitic olivine, and O_2 and SiO are likely by-products formed simultaneously with npFe^0 during this reaction. Combined with the EELS O spectra and EDX Si maps, the vesicle positions within the npFe^0 particles consistently exhibit O-rich features, with some vesicle positions showing an enrichment in Si, which could reflect the characteristics of the gas component. In addition, no helium signals were detected in our studied vesicles, such that solar wind implantation is unlikely to be a common cause of all vesicle formation in Chang'E-5 npFe^0. A comprehensive consideration of the chemical reactions and our analysis results indicate that O_2 and SiO are the most likely candidates for the formation of some vesicles within the npFe^0, and the emergence of these vesicles therefore provides potential redox conditions during the npFe^0 formation. The Si-rich amorphous matrix should also provide support for the decomposition of mafic silicate, and the appearance of an Mg-rich layer is attributed to Fe loss during npFe^0 formation instead of an Mg addition in this layer (Allen et al., 1993; Benzerara et al., 2002; Fazio et al., 2018; Gu et al., 2018; Guo et al., 2020). All of these possible products of olivine decomposition are found in the Chang'E-5 olivine rims, and a reaction to explain the formation of the observed assemblage should be written as that proposed by Leroux et al. (2003).

The optical consequences of $npFe^0$ have been intensively studied in lunar soils as well as in simulation experiments, and different sizes of $npFe^0$ have been found to have quite different spectral alteration effects (Anand et al., 2004; Chapman, 2004; Gaffey, 2010; Hapke, 2001; Noble et al., 2007). In our study, the relatively larger $npFe^0$ (10–35 nm) should have different optical effects from the smaller vapor-deposited $npFe^0$ (~3 nm) found in the rims of Apollo soils. These different-size $npFe^0$ should collectively alter the spectral characteristics of the lunar surface. Therefore, intermediate $npFe^0$ sizes also need to be considered in spectral interpretations of lunar soils, which will help us understand space weathering processes and better interpret the reflectance spectrum obtained by remote sensing.

4.2. Implications for Lunar Surface Conditions

The chemical heterogeneity observed in the uppermost layer of the studied olivine grain rims invokes the occurrence of Si-Fe-Mg interdiffusion in olivine. Such diffusion should have occurred during one or several brief heating events (Burgess & Stroud, 2018a). The large rhombus-shaped $npFe^0$ particles observed in this layer are indicative of thermal crystallization conditions, rather than fast-cooling conditions indicated by smaller spherical $npFe^0$ formed by vapor deposition in the Apollo samples. Thermodynamic calculations show that olivine decomposition reactions occur at temperatures below the melting point, and an increased vacuum degree will reduce the temperature required for olivine decomposition (Figure S8 in Supporting Information S1). The lunar air environment is extremely high vacuum, and its atmospheric pressure is estimated to be approximately 12 orders of magnitude lower than that of the Earth (Heiken et al., 1991). Under normal lunar vacuum conditions (~10^{-9} Pa), the temperature required for olivine decomposition to form SiO_2, SiO, and O_2 is approximately 1,090°C. Under thermal lunar conditions, the reaction temperature decreases with increasing vacuum degree, from 1,030 °C at 10^{-10} Pa to 930 °C at 10^{-12} Pa, which suggests that olivine decomposition can occur at temperatures below the olivine melting point.

The widespread presence of α-iron and absence of melting layers support that the decomposition reaction of the uppermost layer on the studied olivines should occur in the subsolidus state. The temperature at which olivine decomposition occurs within “dusty olivine” (i.e., olivine grain containing abundant tiny metal inclusions) is also considered to be below the melting point of olivine (Leroux et al., 2003).

Considering the Apollo sample results, the (micro)meteorite impact effects on younger Chang'E-5 lunar soils during exposure (less than 100 Ma) should be relatively low (Keller & McKay, 1993, 1997; Yamada et al., 1999). Significant solar flare tracks in the host olivines indicate that these grains have an exposure history and also proves that an extensive postheating event did not occur, which would have eliminated these tracks. Moreover, the random size (<10 nm) and spatial position distributions of the vesicles within the $npFe^0$ suggest that the bubble pressures were not at equilibrium and require a limited exposure age and weaker heating episodes to retain these vesicles. These microscopic features collectively reflect that the studied Chang'E-5 grains did not experience extensive heating events after expose to the lunar surface, and that the features of the uppermost layer on the olivine rims most likely formed before these particles exposed to space.

Decomposition reactions occurred only in the uppermost layer of the olivine grains, suggesting that the heating conditions should have been concentrated only on the lunar soil surfaces. This feature could not have been achieved by large-impact compressional heating or extensive magmatic activity reheating events. It is well known that heating effects acting directly on the lunar surface tend to be dominated by (micro)impacts. The absence of typical melting and vapor deposition layers in the Chang'E-5 grain rims indicates that they were not formed under the same conditions as those experienced by the Apollo samples. For the subsolidus temperature requirement, one possible heating source is frictional heating at the fracture interface during (micro)impact-induced fragmentation; relatively low-velocity micrometeoroid bombardments could also produce local heating events promoting the subsolidus decomposition of olivine. In summary, we conclude that the fragmentation process during (micro) impacts is the most likely scenario for the formation of such common microstructures in the Chang'E-5 soils, and the local heating effects from micrometeoroid impacts cannot be excluded. Furthermore, the uppermost chemical layer structure in the Chang'E-5 olivine rims was not modified by subsequent space weathering (solar wind dominated) processes.

4.3. Space Weathering Effects

Micrometeoroid bombardment and solar wind irradiation are both important agents of space weathering. The Chang'E-5 lunar soils have been shown to be mature in terms of space weathering based on their particle size distribution (Li et al., 2022). The thickness of the solar wind rim and the density of the solar flare tracks observed in our study also suggest that the Chang'E-5 grains are mature. Combined with the relatively younger exposure age of the Chang'E-5 samples, it is apparent that significant space weathering takes place very quickly on the lunar surface (O'Brien & Byrne, 2021).

Solar wind plays an important role in space weathering processes on airless bodies, mainly including the implantation of a significant amount of hydrogen and helium into the topmost surface of these bodies, which causes a partial to complete amorphization of the host crystalline grains (Burgess & Stroud, 2018b; Keller & McKay, 1997). A solar wind component (helium) has been directly identified in the vesicles of the lunar soil in previous studies, which provides direct evidence of the influence of solar wind on the lunar soil (Burgess & Stroud, 2018b; Greer et al., 2020). However, most vesicles found in the rims of the studied olivines are likely to be filled with decomposition products (SiO and O_2). Although no solar wind component was detected in our analyzed vesicles, it cannot be concluded that solar wind-induced vesicles did not exist on the olivine rims. The partially amorphous layers on the olivine rims show an irregular boundary with the underlying host grains, and their depth is consistent with the penetration depth of solar ions (Figure 2b; Carrez et al., 2002). These features suggest that solar wind irradiation dominates Chang'E-5 soils surface alteration during space exposure. Main-belt asteroids have low surface gravities and short exposure times, thus resulting in a low impact product retention rate. The younger Chang'E-5 samples should therefore show more similar space weathering (solar wind dominated) features to those of main-belt asteroids than to those of the Apollo lunar soil samples (Noble et al., 2005; Noguchi et al., 2011).

Moreover, the alteration of the Chang'E-5 soils by micrometeoroid bombardment is very limited, that is, the studied olivine grain rims have no melting layers and lack vapor-deposited material; this is in contrast to the Apollo samples, which experienced intense micrometeorite alteration (Li et al., 2022). Such repeated and frequent impacts from micrometeoroids, altering the lunar surface through shattering and local heating, could be a possible heating source for the formation of $npFe^0$ by subsolidus decomposition of olivine in our study. Furthermore, a weaker micrometeoroid bombardment would allow the distinct chemical layer structure in the Chang'E-5 grain rims to be preserved.

Note that the olivine grains we studied all have a high iron content and show significantly different space weathering effects from that of forsteritic olivine. Most of the olivine grains in the Apollo samples are magnesian (e.g., magnesian mare basalt and Mg-suite rocks), and the space weathering simulation experiments were performed on forsterite-rich olivine grains (Fazio et al., 2018; Heiken et al., 1991). However, recent meteorite studies have indicated that ferroan rocks should distribute on the lunar surface (Gross et al., 2014). Therefore, how Fe-rich components on the lunar surface respond to space weathering processes and how this further affects the reflectance spectrum needs to be considered.

5. Summary

The coexistence of $npFe^0$, SiO, O_2, and SiO_2 phases in the uppermost layer of the Chang'E-5 fayalitic olivine rims is an indicator of the decomposition reaction that acted on the lunar surface. The impact-induced heating processes are invoked to explain the formation of $npFe^0$ under subsolidus conditions. Such unique microstructure of uppermost layer on the Chang'E-5 fayalitic olivine is very different from that of Mg-rich olivine in Apollo samples, revealing the diversity of space weathering effects on the lunar surface. A more detailed understanding of the $npFe^0$ formation mechanism from the newly returned samples provides important information for unraveling the reflectance spectrum changes on airless bodies.

Data Availability Statement

The original TEM and EELS data used in this study are available in Guo (2022).

Acknowledgments
G. Z. analyzed the data sets and wrote the manuscript. L. C. contributed to thermodynamic calculations. L. Y. contributed to the experimental design and manuscript discussion. W. Y. Y. contributed to the preparation of FIB foils. T. K. R., L. X. Y., L. J. Z., and O. Y. Z. Y. contributed to the manuscript discussions. The authors declare that they have no competing interests. We thank CNSA for providing access to the Lunar Sample CE5C0400Y-JFM00505. The authors also would like to thank funding support from the Strategic Priority Research Program of the Chinese Academy of Sciences (Grant XDB 41000000), Natural Science Foundation of China (Grant 41931077), Technical Advanced Research Project of Civil Space (Grant D020201), Youth Innovation Promotion Association CAS (Grant 2020395), and Key Research Program of Frontier Sciences, CAS (Grants ZDBS-SSW-JSC007-10 and QYZDY-SSW-DQC028), Guangxi Scientific Base and Talent Special Projects (No. 1850007 CE).

References

Allen, C. C., Morris, R. V., Lauer, H. V., & McKay, D. S. (1993). Microscopic iron metal ON glass and minerals—A tool for studying regolith maturity. *Icarus*, *104*, 291–300. https://doi.org/10.1006/icar.1993.1102

Anand, M., Taylor, L. A., Nazarov, M. A., Shu, J., Mao, H. K., & Hemley, R. J. (2004). Space weathering on airless planetary bodies: Clues from the lunar mineral hapkeite. *Proceedings of the National Academy of Sciences of the United States of America*, *101*, 6847–6851. https://doi.org/10.1073/pnas.0401565101

Basu, A. (2005). Nanophase Fe-0 in lunar soils. *Journal of Earth System Science*, *114*, 375–380. https://doi.org/10.1007/bf02702956

Benzerara, K., Guyot, F., Barrat, J. A., Gillet, P., & Lesourd, M. (2002). Cristobalite inclusions in the Tatahouine achondrite: Implications for shock conditions. *American Mineralogist*, *87*, 1250–1256. https://doi.org/10.2138/am-2002-8-925

Burgess, K. D., & Stroud, R. M. (2018a). Coordinated nanoscale compositional and oxidation state measurements of lunar space-weathered material. *Journal of Geophysical Research: Planets*, *123*, 2022–2037. https://doi.org/10.1029/2018JE005537

Burgess, K. D., & Stroud, R. M. (2018b). Phase-dependent space weathering effects and spectroscopic identification of retained helium in a lunar soil grain. *Geochimica et Cosmochimica Acta*, *224*, 64–79. https://doi.org/10.1016/j.gca.2017.12.023

Carrez, P., Demyk, K., Cordier, P., Gengembre, L., Grimblot, J., D'Hendecourt, L., et al. (2002). Low-energy helium ion irradiation-induced amorphization and chemical changes in olivine: Insights for silicate dust evolution in the interstellar medium. *Meteoritics & Planetary Science*, *37*, 1599–1614. https://doi.org/10.1111/j.1945-5100.2002.tb00814.x

Chapman, C. R. (2004). Space weathering of asteroid surfaces. *Annual Review of Earth and Planetary Sciences*, *32*, 539–567. https://doi.org/10.1146/annurev.earth.32.101802.120453

Fazio, A., Harries, D., Matthaus, G., Mutschke, H., Nolte, S., & Langenhorst, F. (2018). Femtosecond laser irradiation of olivine single crystals: Experimental simulation of space weathering. *Icarus*, *299*, 240–252. https://doi.org/10.1016/j.icarus.2017.07.025

Gaffey, M. J. (2010). Space weathering and the interpretation of asteroid reflectance spectra. *Icarus*, *209*, 564–574. https://doi.org/10.1016/j.icarus.2010.05.006

Garvie, L. A. J., & Buseck, P. R. (1998). Ratios of ferrous to ferric iron from nanometre-sized areas in minerals. *Nature*, *396*, 667–670. https://doi.org/10.1038/25334

Greer, J., Rout, S. S., Isheim, D., Seidman, D. N., Wieler, R., & Heck, P. R. (2020). Atom probe tomography of space-weathered lunar ilmenite grain surfaces. *Meteoritics & Planetary Science*, *55*, 426–440. https://doi.org/10.1111/maps.13443

Gross, J., Treiman, A. H., & Mercer, C. N. (2014). Lunar feldspathic meteorites: Constraints on the geology of the lunar highlands, and the origin of the lunar crust. *Earth and Planetary Science Letters*, *388*, 318–328. https://doi.org/10.1016/j.epsl.2013.12.006

Gu, L. X., Zhang, B., Hu, S., Noguchi, T., Hidaka, H., & Lin, Y. T. (2018). The discovery of silicon oxide nanoparticles in space-weathered of Apollo 15 lunar soil grains. *Icarus*, *303*, 47–52. https://doi.org/10.1016/j.icarus.2017.12.028

Guo, Z. (2022). *"Original data for the manuscript entitled "Nanophase iron particles derived from olivine decomposition in Chang'e-5 lunar soil: Implications for thermal effects during impacts"", Mendeley Data, V2*. https://doi.org/10.17632/c44477pxc7.2

Guo, Z., Li, Y., Chen, H. Y., Zhang, M. M., Wu, Y. X., Hui, B., et al. (2021). Evidence for the disproportionation of iron in a Eucrite meteorite: Implications for impact processes on Vesta. *Journal of Geophysical Research: Planets*, *126*, e2020JE006816. https://doi.org/10.1029/2020JE006816

Guo, Z., Li, Y., Liu, S., Xu, H. F., Xie, Z. D., Li, S. J., et al. (2020). Discovery of nanophase iron particles and high pressure clinoenstatite in a heavily shocked ordinary chondrite: Implications for the decomposition of pyroxene. *Geochimica et Cosmochimica Acta*, *272*, 276–286. https://doi.org/10.1016/j.gca.2019.10.036

Hapke, B. (2001). Space weathering from Mercury to the asteroid belt. *Journal of Geophysical Research: Planets*, *106*, 10039–10073. https://doi.org/10.1029/2000JE001338

Hapke, B., Cassidy, W., & Wells, E. (1975). Effects of vapor-phase deposition processes on optical, chemical, and magnetic-properties of lunar regolith. *The Moon*, *13*, 339–353. https://doi.org/10.1007/BF00567525

Heiken, G., Vaniman, D. T., & French, B. M. (1991). *Lunar sourcebook—A user's guide to the moon*. Cambridge University Press.

Keller, L. P., & Mckay, D. S. (1993). Discovery of vapor deposits in the lunar regolith. *Science*, *261*, 1305–1307. https://doi.org/10.1126/science.261.5126.1305

Keller, L. P., & McKay, D. S. (1997). The nature and origin of rims on lunar soil grains. *Geochimica et Cosmochimica Acta*, *61*, 2331–2341. https://doi.org/10.1016/s0016-7037(97)00085-9

Leroux, H., Libourel, G., Lemelle, L., & Guyot, F. (2003). Experimental study and TEM characterization of dusty olivines in chondrites: Evidence for formation by in situ reduction. *Meteoritics & Planetary Science*, *38*, 81–94. https://doi.org/10.1111/j.1945-5100.2003.tb01047.x

Li, C., Hu, H., Yang, M. F., Pei, Z. Y., Zhou, Q., Ren, X., et al. (2022). Characteristics of the lunar samples returned by the Chang'E-5 mission. *National Science Review*, *9*(2), nwab188. https://doi.org/10.1093/nsr/nwab188

Loeffler, M. J., Dukes, C. A., & Baragiola, R. A. (2009). Irradiation of olivine by 4 keV He+: Simulation of space weathering by the solar wind. *Journal of Geophysical Research*, *114*, E03003. https://doi.org/10.1029/2008JE003249

Noble, S. K., Keller, L. P., & Pieters, C. M. (2005). Evidence of space weathering in regolith breccias I: Lunar regolith breccias. *Meteoritics & Planetary Science*, *40*, 397–408. https://doi.org/10.1111/j.1945-5100.2005.tb00390.x

Noble, S. K., Pieters, C. M., & Keller, L. P. (2007). An experimental approach to understanding the optical effects of space weathering. *Icarus*, *192*(2), 629–642. https://doi.org/10.1016/j.icarus.2007.07.021

Noble, S. K., Pieters, C. M., Taylor, L. A., Morris, R. V., Allen, C. C., McKay, D. S., & Keller, L. P. (2001). The optical properties of the finest fractio n of lunar soil: Implications for space weathering. *Meteoritics & Planetary Science*, *36*, 31–42. https://doi.org/10.1111/j.1945-5100.2001.tb01808.x

Noguchi, T., Kimura, M., Hashimoto, T., Konno, M., Nakamura, T., Zolensky, M. E., et al. (2014). Space weathered rims found on the surfaces of the Itokawa dust particles. *Meteoritics & Planetary Science*, *49*, 188–214. https://doi.org/10.1111/maps.12111

Noguchi, T., Nakamura, T., Kimura, M., Zolensky, M. E., Tanaka, M., Hashimoto, T., et al. (2011). Incipient space weathering observed on the surface of Itokawa dust particles. *Science*, *333*, 1121–1125. https://doi.org/10.1126/science.1207794

O'Brien, P., & Byrne, S. (2021). Physical and chemical evolution of lunar mare regolith. *Journal of Geophysical Research: Planets*, *126*, e2020JE006634. https://doi.org/10.1029/2020JE006634

Pieters, C. M., Fischer, E. M., Rode, O., & Basu, A. (1993). Optical effects of space weathering—The role of the finest fraction. *Journal of Geophysical Research: Planets*, *98*, 20817–20824. https://doi.org/10.1029/93JE02467

Pieters, C. M., & Noble, S. K. (2016). Space weathering on airless bodies. *Journal of Geophysical Research: Planets*, *121*, 1865–1884. https://doi.org/10.1002/2016JE005128

Qian, Y., Xiao, L., Head, J. W., Wöhler, C., Bugiolacchi, R., Wilhelm, T., et al. (2021). Copernican-aged (<200 Ma) impact Ejecta at the Chang'e-5 landing site: Statistical evidence from crater morphology, morphometry, and degradation models. *Geophysical Research Letters*, *48*, e2021GL095341. https://doi.org/10.1029/2021GL095341

Sasaki, S., Nakamura, K., Hamabe, Y., Kurahashi, E., & Hiroi, T. (2001). Production of iron nanoparticles by laser irradiation in a simulation of lunar-like space weathering. *Nature*, *410*, 555–557. https://doi.org/10.1038/35069013

Thompson, M., Barnes, J., Blewett, D., Cahill, J., Denevi, B., Donaldson Hanna, K., et al. (2021). Space weathering across the solar system: Lessons from the moon and outstanding questions. *Bulletin of the American Astronomical Society*, *53*(4), 172. https://doi.org/10.3847/25c2cfeb.0bd09213

van de Moortele, B., Reynard, B., Rochette, P., Jackson, M., Beck, P., Gillet, P., et al. (2007). Shock-induced metallic iron nanoparticles in olivine-rich Martian meteorites. *Earth and Planetary Science Letters*, *262*, 37–49. https://doi.org/10.1016/j.epsl.2007.07.002

Weber, I., Stojic, A. N., Morlok, A., Reitze, M. P., Markus, K., Hiesinger, H., et al. (2020). Space weathering by simulated micrometeorite bombardment on natural olivine and pyroxene: A coordinated IR and TEM study. *Earth and Planetary Science Letters*, *530*, 115884. https://doi.org/10.1016/j.epsl.2019.115884

Yamada, M., Sasaki, S., Nagahara, H., Fujiwara, A., Hasegawa, S., Yano, H., et al. (1999). Simulation of space weathering of planet-forming materials: Nanosecond pulse laser irradiation and proton implantation on olivine and pyroxene samples. *Earth Planets Space*, *51*, 1255–1265.